


ARTICLE

<https://doi.org/10.1038/s42005-019-0173-1>

OPEN

Enhanced photo-sensitivity in a Si photodetector using a near-field assisted excitation

T. Yatsui¹, S. Okada¹, T. Takemori¹, T. Sato¹, K. Saichi¹, T. Ogamoto¹, S. Chiashi¹, S. Maruyama^{1,2} , M. Noda³, K. Yabana³, K. Iida⁴ & K. Nobusada⁴

Silicon is an indispensable material in electric device technology. However, Si is an indirect bandgap material; therefore, its excitation efficiency, which requires phonon assistance, is low under propagating far-field light. To improve the excitation efficiency, herein we performed optical near-field excitation, which is confined in a nano-scale, where the interband transitions between different wave numbers are excited according to the uncertainty principle; thus, optical near-field can directly excite the carrier in the indirect bandgap. To evaluate the effect of optical near-field confined in a nano-scale, we fabricate the lateral Si p-n junction with Au nanoparticles as sources to generate the field confinement. We observed a 47.0% increase in the photo-sensitivity rate. In addition, by using the thin lateral p-n junction, which eliminates the far-field excitation, we confirmed a 42.3% increase in the photo-sensitivity rate.

¹School of Engineering, The University of Tokyo, 7-3-1 Hongo, Bunkyo 113-8656, Japan. ²Energy NanoEngineering Lab, National Institute of Advanced Industrial Science and Technology (AIST), 1-2-1 Namiki, Tsukuba 305-8564, Japan. ³Center for Computational Sciences, University of Tsukuba, 1-1-1 Tennodai, Tsukuba 305-8577, Japan. ⁴Department of Theoretical and Computational Molecular Science, Institute for Molecular Science, 38 Nishigo-Naka, Myodaiji, Okazaki 444-8585, Japan. Correspondence and requests for materials should be addressed to T.Y. (email: yatsui@lux.t.u-tokyo.ac.jp)

Si is one of the most important materials in electric device technology. However, because Si is an indirect bandgap material, phonon assistance is required to excite the carriers from the Γ point to the X point in photo-excitation^{1,2} (refer to Fig. 1a), which results in a low excitation efficiency while using a propagating far field (FF). To improve the excitation efficiency, many researchers utilize the enhancement of the optical-field intensity through the plasmon resonance^{3–5}. Further improvement of the photo-excitation is realized using a photonic design to induce light trapping with three-dimensional structures⁶. Although the absorption efficiency was improved by the increase in the electric-field intensity, they continue to require phonon assistance. A direct excitation of Si without phonon assistance is expected to be realized by using the optical near-field (ONF), which is confined in a nano-scale^{7–9}. Owing to the localization of the optical field at the nano-scale (i.e., a very small value of Δx), large components of wave numbers (a large value of Δk) are generated according to the uncertainty principle (Fig. 1b). Although a large value of Δk can be generated by plasmon excitation, it should be noted that the large-wave-numbers generation requires field confinement only¹⁰. In contrast, field enhancement realized by the plasmon excitation requires field confinement¹¹, as well as a negative value for permittivity to meet the condition of plasmon resonance¹². In other words, a large value of Δk can be generated without plasmon excitation. A numerical calculation considering the ONF source revealed that ONFs had Fourier components with large wave numbers caused by the non-uniformity of the electric field. The thorough time-dependent dynamics calculations of a one-dimensional periodic potential with an indirect band-gap structure demonstrated herein that the ONF induced an indirect transition without phonon assistance⁸. It was also found that the direct optical transition by ONF in realistic Si system can induce a sufficiently large absorption intensity (larger than the simple model system), where the source of ONF was treated as a point dipole¹⁰. There were no realistic metallic structures in the system that could generate plasmons. Thus, the direct optical transition by ONF does not require phonon assistance and can realize direct excitation exclusively with photons. Therefore, by considering the

generation of the large wave number from the ONF together with the plasmonic effect, we expected further device improvement.

To evaluate the effect of ONF confined in a nano-scale, we fabricated the Si photodetector composed of lateral p-n junction with Au nanoparticles as the ONF source at the p-n junction surface.

Results

Lateral p-n junction with Au nanoparticles. To evaluate the effect of ONF in photo-excitation, because the size of ONF is in the nano-scale, we fabricated the lateral p-n junction, such that the p-n junction is located at the surface of the device. Using lithography, we fabricated lateral the p-n junction from an n-type Si wafer with dopant density of 10^{15} cm^{-3} . p-type Si was prepared via thermal diffusion of boron. For the boron source, we used B153 of spin on dopant (SOD) (Filmtronics). The density of dopant was estimated as 10^{20} cm^{-3} with a thickness of $0.9 \mu\text{m}$ (Fig. 2a)¹³. From the dopant densities of the p-type and n-type Si, the depletion layer thickness in the n-type Si was estimated as $1.06 \mu\text{m}$. After the deposition of thin Cr, 200-nm-thick Au was deposited as the electrode. In addition, to increase the carriers' density at the surface of the p-n junction and subsequently raise the detection efficiency of the excited carriers, we fabricated a p-n junction in the comb structure (Fig. 2b, c). Finally, Au nanoparticles (Tanaka Kikinzoku Kogyo) were dispersed on the Si p-n junction (inset, Fig. 2d). The solution containing the Au

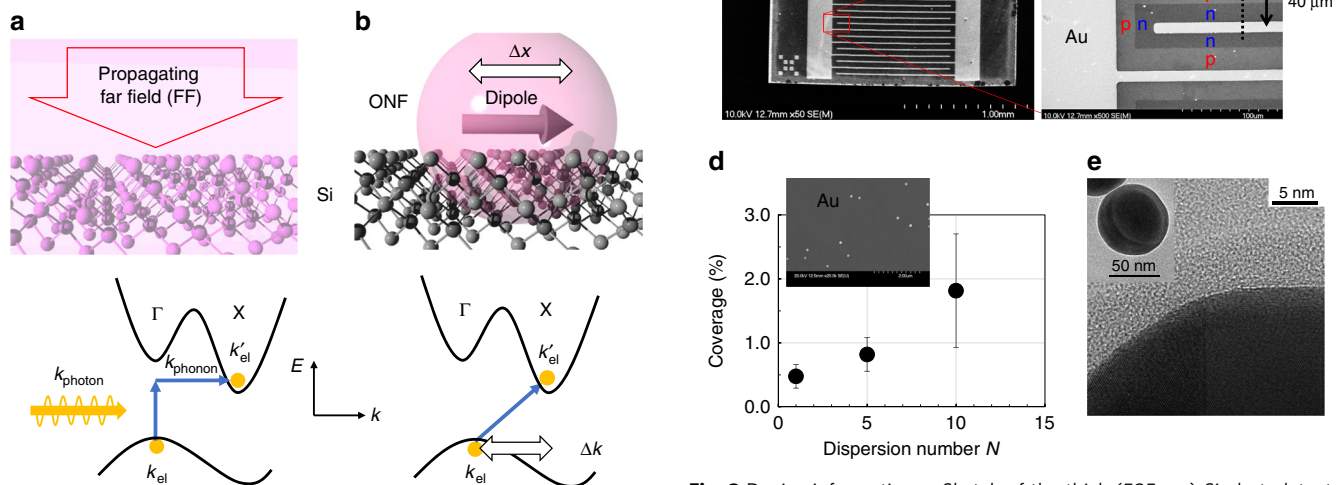


Fig. 2 Device information. **a** Sketch of the thick ($525 \mu\text{m}$) Si photodetector with a lateral p-n junction. The thickness of the depletion layer W was estimated as $1.06 \mu\text{m}$. d : the thickness of p-doped layer. **b** Scanning electron microscopic (SEM) picture of the fabricated Si detector. **c** Magnified SEM picture of **b**. **d** Dispersion number N dependence of the Au nanoparticle (diameter of 100 nm) coverage. Inset: SEM image of the dispersed Au nanoparticles with $N = 5$ (diameter of 100 nm). The error bar corresponds to the standard deviation of the coverage. **e** Transmission electron microscopic (TEM) image of the Au nanoparticle

nanoparticles was dispersed on the Si device and the solvent was evaporated by heating at 75 °C using a hot plate for 1 min. We counted this procedure of the dispersion number N as one and repeated it depending on the experiment. Figure 2d shows the Au nanoparticle coverage as a function of N . The Au nanoparticle had a spherical shape, as shown in the transmission electron microscopic (TEM) image in Fig. 2e. Therefore, we considered that there is a distinct boundary at the interface between the Au nanoparticle and Si substrate.

Photo-sensitivity measurement. To evaluate the effect of the ONF in photo-excitation, we compared the photo-sensitivity of the lateral p–n junction with and without Au nanoparticles. We obtained wavelength dependence of the photo-sensitivity using a white light source (halogen lamp). The photo-sensitivity [A W^{-1}] was obtained from the relation between the detected photo-current and the incident power. We first obtained the photo-sensitivity without the Au nanoparticles. Then, Au nanoparticles were dispersed on the device. Finally, we obtained the photo-sensitivity at the same position. Figure 3a shows the sensitivity of the thick Si device with 525 μm of Si substrate (Fig. 2a) for three

samples. The solid red circles in Fig. 3a represent the thick device with 100-nm Au nanoparticles (dispersion number, $N = 5$). From the obtained sensitivity, we obtained the increased photo-sensitivity rate for $N = 1, 5$, and 10 (Fig. 3b), in which the photo-sensitivity with Au nanoparticles was normalized by the photo-sensitivity without Au nanoparticles. These results showed that the rate increased as N increased (i.e., 47.0% at $\lambda = 1100$ nm and $N = 10$). In addition, the increased photo-current rate increased for the longer wavelength. Although the 100-nm Au nanoparticle in air has an absorption peak at around 520 nm due to the plasmon resonance¹⁴, the peak could shift because of the substrate.

To exclude the red shift in the absorption spectra caused by the substrate, we compared the scattering cross-section of the 100-nm Au spherical nanoparticle in air and on the Si substrate. We performed the numerical calculation using the finite difference time domain (FDTD) method¹⁵. We then calculated the scattering cross-section of the spherical Au nanoparticle with 100 nm diameter in air and set on the Si substrate ($600 \times 600 \times 2400$ nm, see Fig. 3c). We calculated the fields without the Au nanoparticle as a reference. To calculate the scattering cross-section, a light source with a uniform electric field intensity in the

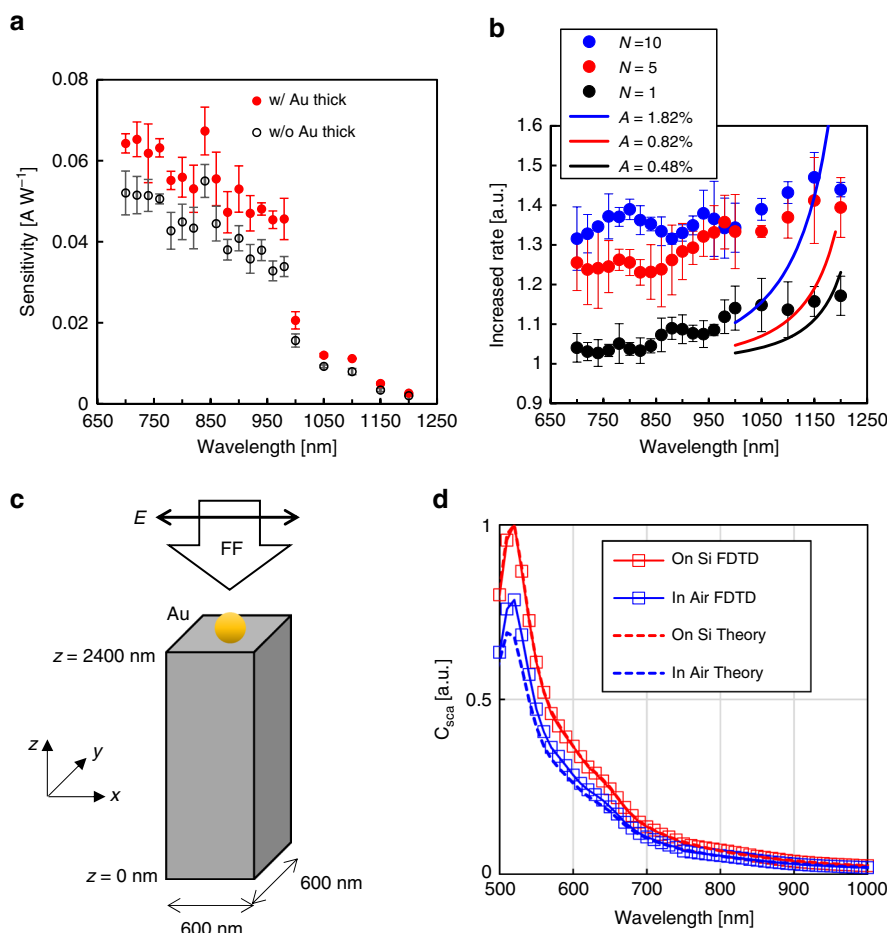


Fig. 3 Sensitivity of thick Si device and scattering cross-section. **a** Sensitivity of thick Si device as a function of the excitation wavelength. The solid red circles represent the thick device with 100-nm Au nanoparticles (dispersion number, $N = 5$). The open black circles represent the thick device before the Au nanoparticle dispersion. The error bar corresponds to the standard deviation of the sensitivity for three samples. **b** Increased photo-sensitivity rate as a function of the excitation wavelength for $N = 1, 5$, and 10. The solid curves represent the calculated increased rate using Eq. (5) with the ratios of the direct transition $A = 1.82\%$ (blue, $N = 10$), 0.82% (red, $N = 5$), and 0.48% (black, $N = 1$). The error bar corresponds to the standard deviation of the increased rate for three samples. **c** Sketch of the calculation model for the finite difference time domain (FDTD). FF: far-field. **d** Calculated scattering cross-section C_{sca} . The solid lines and open squares indicate the FDTD results on Si (red) and in air (blue), respectively. The dashed lines denote the calculated results using Eq. (3) on Si (red) and in air (blue).

xy -plane was used, which was a differential Gaussian wave in the time domain with a wavelength calculation range between 400 and 1300 nm. The angle resolution to calculate the scattering cross-section was set to 5° ¹⁶.

The solid lines in Fig. 3d show the normalized scattering cross-section. The calculated results indicated that the Au nanoparticle spectra both in air and on the Si substrate reached a maximum at 520 nm because of the plasmon resonance. The intensity on the Si substrate (solid red line, Fig. 3d) increased in comparison with that in air (solid blue line, Fig. 3d); however, the peak wavelength remained the same for both cases. The intensity increase on the substrate should originate from the mirror image effect. To support this, we also calculated the scattering cross-section using the dipole approximation¹⁷. The polarizability of the Au sphere on the Si substrate is determined as:

$$\chi = \frac{\epsilon_{\text{Air}}(\epsilon_{\text{Au}} - \epsilon_{\text{Air}})V}{\epsilon_{\text{Air}} + L(\epsilon_{\text{Au}} - \epsilon_{\text{Air}})}, \quad (1)$$

where ϵ_{Au} and ϵ_{Air} are the permittivity of gold and air, respectively, and V is the volume of the Au sphere. Parameter L is defined as:

$$L = \frac{1}{3} \left(1 - \frac{1}{8} \frac{\epsilon_{\text{Si}} - \epsilon_{\text{Air}}}{\epsilon_{\text{Si}} + \epsilon_{\text{Air}}} \right), \quad (2)$$

where ϵ_{Si} is the Si permittivity. We considered the mirror dipole in the Si substrate in this model. The scattering cross-section is obtained as:

$$C_{\text{sca}} = \frac{k^4}{6\pi} |\chi|^2, \quad (3)$$

where k is the wave number, and χ is obtained using Eqs. 1, 2. We calculated the scattering cross-section (dashed lines, Fig. 3d) using the formula. The results showed that the FDTD spectra were well fitted by Eq. 3, indicating that the intensity increase on the Si substrate originated from the mirror image effect. Although many researchers have reported the red shift by the ellipsoid shape (not the spherical shape)^{18,19}, it is reasonable to exclude the effect of the plasmon enhancement from the reason for the photo-excitation enhancement observed here because our Au nanoparticle had a nearly spherical shape. As shown in Fig. 2d, the coverage of the Au nanoparticles was estimated to be as small as 1.8%. The small increase in the photo-sensitivity rate might be caused by the inadequate coverage of Au nanoparticles.

Several groups have realized the sensitivity increase using metallic nanoparticles, however, the metallic coverage in their experiment was estimated to be more than 50%^{18,20,21}. Such a high-density metallic nanoparticle reported in the literatures^{18,20,21} induced light scattering and resulted in a longer optical pass in the detector. As discussed in Supplementary Note 1, the isolated metallic nanoparticle did not induce the strong light scattering. Furthermore, we can exclude the light scattering effect because the scattering intensity depended on λ^{-4} .

The absorption coefficient of the indirect bandgap material α_i near the energy band gap E_g depended on $\alpha_i \propto (h\nu - E_g)^2/h\nu$ (h is the Planck constant, ν is the frequency), while that of the direct bandgap material α_D depended on $\alpha_D \propto (h\nu - E_g)^{1/2}/h\nu$ ²². The bias voltage in our experiment was 0; thus, the photo-current should be the same as the short circuit current²³:

$$I_{\text{SC}} = Q(1 - r)\{1 - \exp(-\alpha l)\}en, \quad (4)$$

where Q is the collection efficiency, r is the reflection coefficient, l is the absorbing layer thickness, e is the electron charge, and n is the number of photons per second per unit of the p-n junction. We expect herein that the ONF can realize the direct transition by

generating a large wave number in the vicinity of Au nanoparticles. Thus, the photo-current for the device with the Au nanoparticles consisted of the current that originated from the direct transition $I_{\text{SC,D}}$ and that from the indirect transition $I_{\text{SC,I}}$. The increased rate in the current device could be expressed as follows if the respective ratios of the direct and indirect transitions are A and $(1 - A)$:

$$\begin{aligned} \frac{AI_{\text{SC,D}} + (1 - A)I_{\text{SC,I}}}{I_{\text{SC,I}}} &= \frac{A(1 - \exp(-\alpha_D l)) + (1 - A)(1 - \exp(-\alpha_I l))}{1 - \exp(-\alpha_I l)} \\ &\approx \frac{(A\alpha_D + (1 - A)\alpha_I)l}{\alpha_I l} \\ &= C \frac{A(h\nu - E_g)^{1/2} + (1 - A)(h\nu - E_g)^2}{(h\nu - E_g)^2} \end{aligned} \quad (5)$$

where we used the Taylor series of the exponential function, and C is the proportional constant. The solid curves in Fig. 3b denoted the calculated increased rate using Eq. 5. In the calculation, E_g was set to 0.96 eV, which was an average value of $N = 1, 5$, and 10 obtained from fitting by the relation $I_{\text{SC,I}} \propto \alpha_i \propto (h\nu - E_g)^2/h\nu$ for the photo-sensitivity data (Fig. 3a). The value of $E_g = 0.96$ eV, as the band gap of Si, is smaller than that of Si (1.1 eV). However, the decrease in the band gap energy originates from the band narrowing due to heavy doping, as high as 10^{20} cm^{-3} ²⁴. Because we considered the relation around the band edge wavelength, furthermore we evaluated the wavelength dependence of the increased rate between 700 and 1200 nm, the calculated wavelength ranged between 1000 and 1200 nm. The ratios of the direct transition A were set to 0.48, 0.82, and 1.82% for the average coverage of $N = 1, 5$, and 10, respectively. The difference in the wavelength dependence of the increased rate between the experimental and calculated ones was caused by the narrow depletion layer on the Si surface. The Au nanoparticles were randomly deposited on the p-type, n-type, and depletion layers. The width of the depletion layer was only 1.06 μm in contrast to the wide electrode separation of 40 μm . However, the higher increased rate near the band gap energy shown here supported the possibility of the direct transition by the ONF.

Although we realized increased photo-sensitivity by the introduction of the Au nanoparticles, the penetration depth of the Si in the infrared region is estimated to be more than 10 μm , which is longer than the p-layer depth of 0.9 μm . Thus, most of the carriers in the thick photo-detector should be generated in the Si bulk substrate beneath the p-layer, that is, the carrier can be generated due to the FF effect. To eliminate the FF excitation, we prepared a thin lateral p-n junction using an n-type silicon-on-insulator (SOI) with a thickness of 0.9 μm with a dopant density of 10^{13} cm^{-3} (Fig. 4a). The thickness of the buried oxide (BOX) layer in the SOI wafer was 1.5 μm . The p-type layer was also fabricated by the thermal diffusion of boron, so that the dopant density is 10^{20} cm^{-3} . From the dopant densities of the p-type and n-type Si, the depletion layer thickness was estimated as 9.92 μm in the n-type Si. Note that no depletion layer existed beneath the p-layer. The Au nanoparticles were additionally dispersed after device fabrication.

First, we compared the sensitivity between the thick and thin (SOI) devices. Figure 4b shows the sensitivity of thin Si device using a SOI for the three samples. The solid blue circles in Fig. 4b represent the thin device with the dispersion number, $N = 5$, of the 100-nm Au nanoparticles. The results showed a thin device with two times lower sensitivity compared to the thick device, indicating that the thin device could eliminate the FF excitation. Figure 4c shows the increased photo-sensitivity rate as a function

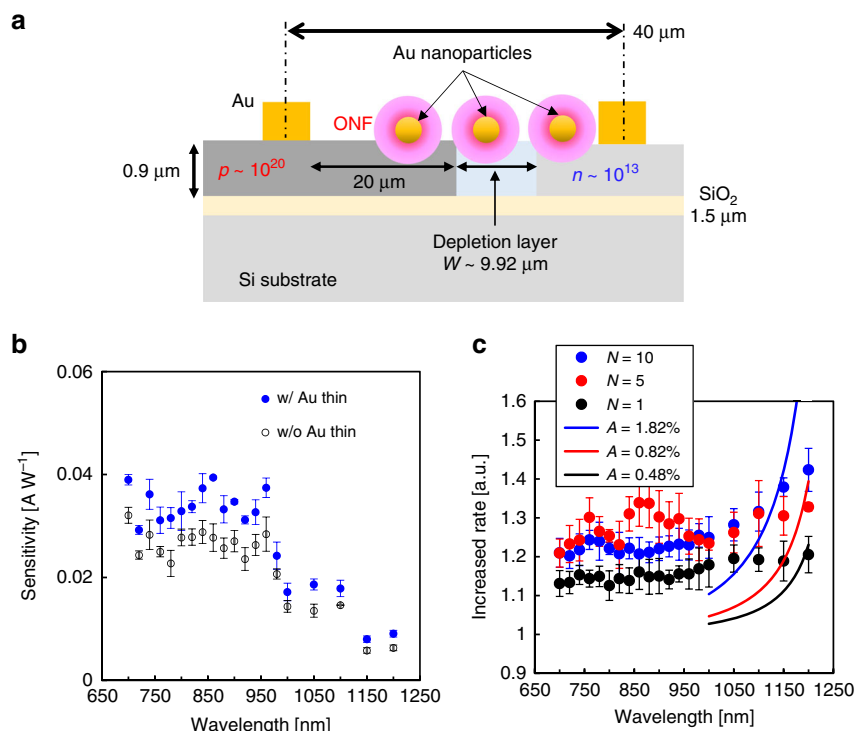


Fig. 4 Sensitivity of thin Si device. **a** Sketch of the thin Si photodetector using a silicon-on-insulator (SOI). W : thickness of the depletion layer. **b** Sensitivity of the thin (SOI) devices as a function of the excitation wavelength. The solid blue circles represent the thin device with the 100-nm Au nanoparticles (dispersion number, $N=5$). The open black circles represent the thin device before the Au nanoparticle dispersion. The error bar corresponds to the standard deviation of the sensitivity for three samples. **c** Increased photo-sensitivity rate as a function of the excitation wavelength for $N=1, 5$, and 10 . The solid curves represent the calculated increased rate using Eq. 5 with the ratios of the direct transition $A=1.82\%$ (blue, $N=10$), 0.82% (red, $N=5$), and 0.48% (black $N=1$). The error bar corresponds to the standard deviation of the increased rate for three samples

of the incident wavelength for $N=1, 5$, and 10 . It should be noted that the increased rate enhanced for the longer wavelength. The solid curves in Fig. 4c show the calculated increased rate using Eq. 5. Although a difference was found in the wavelength dependence of the increased rate between the experimental and calculated ones, the gradient of the increased rate of $N=10$ in the wavelength range from 1000 to 1200 nm was 0.0009 nm^{-1} . This value was approximately 1.8 times larger than that for the thick device of $N=10$ in the same wavelength range. As N increased, the rate increased up to 42.3% at $\lambda=1200$ nm and $N=10$. As the thin lateral p-n junction the FF excitation beneath the p-layer was eliminated, the increase in the photo-sensitivity rate originated exclusively from the field confinement at the surface of the device. A higher photo-sensitivity could be realized by introducing a higher Au nanoparticle density and a larger surface area of the depletion layer, such as a pin junction.

To examine the size dependence of the Au nanoparticles, we compared the increased photo-sensitivity rate with different values of the Au nanoparticle diameter. Figure 5a, b show the diameter dependence of the increased photo-sensitivity for the thick and thin devices, respectively. In this study, N was set to 5 for all diameter samples. Figure 5c shows the increased photo-sensitivity rate at a wavelength of 1100 nm. From the results, it was found that the highest photo-sensitivity was achieved with a Au nanoparticle having a diameter of 100 nm for both devices near the band gap wavelength of 1100 nm.

This size dependence of the larger Au nanoparticles resulting in higher photo-sensitivity did not appear to be consistent with the theory of direct optical transition by the ONF because based on the uncertainty principle of the direct optical transition by the ONF, a greater Δk can be obtained as the nanoparticle size

decreases. To examine the size dependence of the Au nanoparticles, we performed numerical calculations using FDTD method. To calculate the near-field component, we set Au nanoparticles on the Si substrate ($600 \text{ nm} \times 600 \text{ nm} \times 2400 \text{ nm}$, same as Fig. 3c). As described in the Supplementary Information, similar electric-field intensity (Supplementary Fig. 1) and Poynting vector (Supplementary Fig. 2) distributions for the Au nanoparticle on the SOI (Si: $600 \text{ nm} \times 600 \text{ nm} \times 900 \text{ nm}$ on SiO_2 : $600 \text{ nm} \times 600 \text{ nm} \times 1500 \text{ nm}$) were obtained. Therefore, we discuss herein the distribution only on the Si substrate. The unit cell was the same for all the Au nanoparticle sizes. The refractive indexes for Au and Si (same as Si in SOI) were $0.31 + i 7.93$ and 3.54 , respectively. We performed the calculation using continuous wave light source with a wavelength of 1100 nm, in which the light has a linearly polarized light with x -polarization. To calculate the near-field effect, we first calculated the electric-field intensity distribution at the interface between Au nanoparticle and the Si substrate. Figure 6a–e shows the square of electric-field intensity distributions of Au nanoparticles with a diameter of 100 nm. Next, we obtained the wave number by calculating the Fourier transform of the electric field distribution along the x -axis. Figure 6e shows an averaged power spectrum ($0 \leq y \leq D/2$) for different Au nanoparticle sizes. The wave number difference between the Γ point and the point at which the conduction band of Si has the lowest energy (X point) is obtained as $k_{x,\Gamma X} = 0.85 \times \pi/a^{25}$. Using a value of $a = 5.43 \times 10^{-1} \text{ nm}$ for Si, we obtained the value of $k_{x,\Gamma X} = 4.92 \text{ nm}^{-1}$. The red solid circles in Fig. 6f show the intensity of power spectra at $k_{x,\Gamma X} = 4.92 \text{ nm}^{-1}$ in Fig. 6e ($|F(E)_{\Gamma X}|^2$). From the results, the highest intensity was obtained for a diameter of 100 nm, which is more than 10,000 times larger than that for a diameter of 5 nm. The calculated size dependence,

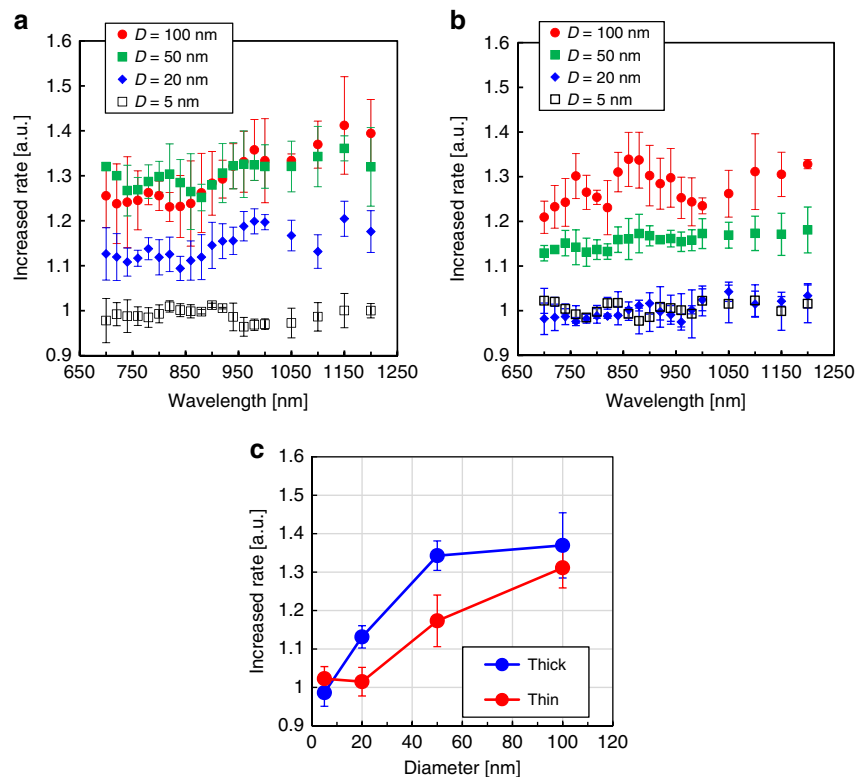


Fig. 5 Comparison of the increased rate on device structures and diameters of the Au nanoparticle. Diameter D of the Au nanoparticle dependence of the increased photo-sensitivity for the **a** thick and **b** thin devices. The error bar corresponds to the standard deviation of the increased rate for three samples. **c** Increased photo-sensitivity rate at a wavelength of 1100 nm. The error bar corresponds to the standard deviation of the increased rate for three samples

taking the maximum at a diameter of 100 nm (Fig. 6f), was consistent with the experimental results shown in Fig. 5c. As shown in Fig. 6a–d, the electric field strongly localized in the interface between the Au nanoparticle and Si; hence, the decrease in the value of $|F(E)_{\text{TX}}|^2$ at $D = 200$ nm should be caused by the absorption in Au. However, the results contradict the prediction from the theory of direct optical transition by the ONF based on the uncertainty principle. To evaluate the effect of generating a larger k -component by the ONF, we calculated the intensity of the normalized power spectra, which was normalized using the square of the volume of Au nanoparticles (open blue circles in Fig. 6f). The large k -component was generated by nanoparticle scattering. Therefore, the Fourier spectral intensity of the electric field, $|F(E)|^2$, should be proportional to the scattering cross-section (proportional to the square of polarizability²⁶). Because polarizability is proportional to the volume²⁷, it is reasonable to normalize $|F(E)|^2$ by r^6 (proportional to the square of volume)¹². Here, the intensity of the normalized power spectra decreased with the increase in size. From the FDTD results, it was confirmed that, when the size decreases, a greater Δk is generated, thereby increasing the efficiency of the direct optical transition by the ONF. In addition, by considering the volume, the photo-sensitivity increases with size.

Discussion

We achieved an enhancement in the photo-excitation efficiency by introducing Au nanoparticles as the ONF sources. Metallic nanoparticles with a significantly low coverage were used here, which were examined in a wavelength range opposite to the plasmon resonance to ensure that the field enhancement was not dominant. Therefore, we believe our results unsealed the possibility of a large Δk generation by field confinement by the ONF sources. Further improvement could be realized if the depletion

area is increased by introducing the intrinsic Si layer between the p-type and n-type layers, i.e., pin diode structure. By using the effect of the near-field excitation shown here, the photodetector and solar cell with a higher efficiency could be realized²⁸. As for the improvement of the photo-excitation in an indirect bandgap material, the band engineering method has been proposed for Ge, in which by introducing the strain, the band diagram turned to be the direct bandgap and resulted in the improvement of the photo-excitation²⁹. Since the possibility of direct transition by the ONF, which is not inherent in Si, it can be utilized in various other applications, including photodetectors, light-emitting devices, H_2 generation, using the indirect bandgap materials including Ge³⁰, SiC³¹, diamond³², and multilayer MoS_2 ^{33,34}.

Methods

Fabrication process of the p–n junction using lithography. We fabricated the device from an n-type Si through the following steps: (i) We prepared the photomask by electron beam lithography. (ii) The Si substrate was cleaned using a piranha solution and an hydrogen fluoride (HF) solution. (iii) The SiO_2 layer with 100 nm for the mask in lithography was prepared by thermal oxidation. (iv) The SiO_2 layer was patterned by photolithography using a photo-resist (ZPN, ZEON Co.). (v) For boron doping for p-type, the boron source of the SOD was coated by spin coating with 3000 rpm for 10 s and baked for 90 s at 100 °C using a hot plate. Boron doping was performed in a furnace at 1000 °C for 120 min with O_2 (0.5 L min^{-1}) and N_2 (1.5 L min^{-1}). (vi) The SiO_2 layer was removed using the HF solution. (vii) The electrode was fabricated through the lift-off technique. A 200-nm-thick Au was deposited by sputtering after the thin Cr later deposition. The resist for the lift-off was removed by acetone through ultrasonic cleaning.

FDTD simulation conditions. The computer simulations herein were performed by an FDTD-based program, Poynting for Optics (Fujitsu, Japan). The boundary conditions were set to a periodic boundary condition (PBC) in the x and y directions and perfectly matched layer (PML) in the z direction. The basic computational area was set to $600 \times 600 \times 9500$ ($-5000 \text{ nm} \leq z \leq 4500$) nm. In this model, the coverage of a 100 nm particle on a 600×600 nm surface was 2.2%, which is comparable to the experimental coverage value of approximately 2%. All light sources with a uniform electric field intensity ($1.0 \text{ [V m}^{-1}\text{]}$) in the xy -plane

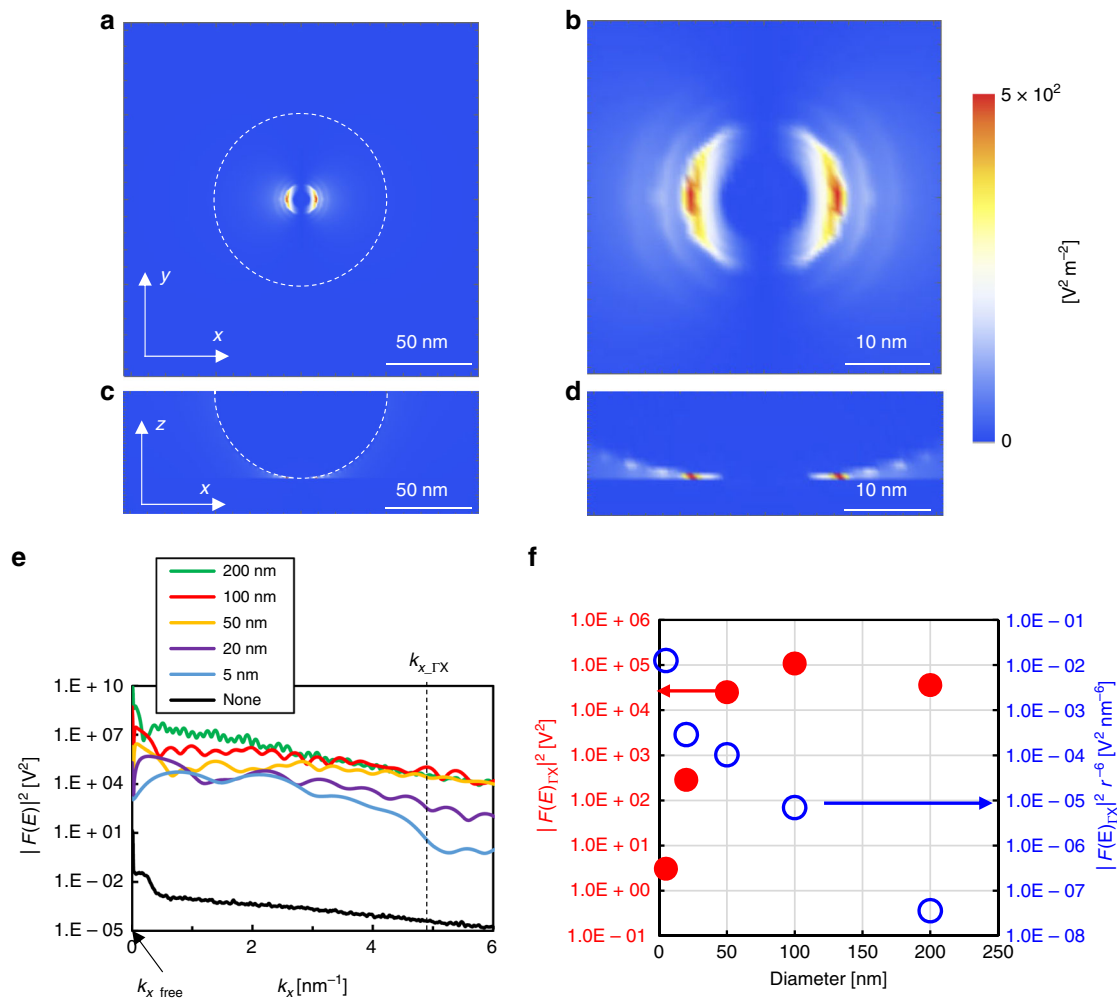


Fig. 6 Numerical evaluation of the near-field assisted excitation. **a–d** Electric-field intensity distribution E^2 at the interface of Au nanoparticle (diameter D of 100 nm) and Si substrate. The dashed white circles in **a** and **c** indicate the Au nanoparticle outline. **e** Averaged Fourier spectrum of the electric-field. k_x : the wave number along the x-axis. The Fourier spectra along the x-axis were averaged as $0 \leq y \leq D/2$. The legends indicate the diameter D of the Au nanoparticles. None (black line) is the case without the Au nanoparticle. $k_{x,\text{free}}$ ($=5.71 \times 10^{-3} [\text{nm}^{-1}]$) is the ideal k -component for the wavelength of 1100 nm in a free space. The value of wave number difference between the Γ point and the point at which the conduction band of Si has the lowest energy (X point) is obtained as $k_{x,\Gamma X} = 4.92 \text{ nm}^{-1}$ was indicated as dashed black line. **f** Red solid circles (left vertical axis) represent the diameter dependence of the power spectrum at $k_{x,\Gamma X} = 4.92 [\text{nm}^{-1}]$, corresponding to the wave number difference between Γ and X points: $|F(E)_{\Gamma X}|^2$. Blue open circles (right vertical axis) represent the normalized value of the $|F(E)_{\Gamma X}|^2$ by the square of the volume: $|F(E)_{\Gamma X}|^2 r^{-6}$

were set at $z = 4200 \text{ nm}$. To calculate the scattering cross-section, a light source that was a differential Gaussian wave in the time domain was used. In the rest of the calculations for the electric-field intensity distributions, the light source was a sinusoidal wave in the time domain. The minimum and maximum grid sizes were $0.22 \times 0.22 \times 0.48 \text{ nm}$ and $10 \times 10 \times 10 \text{ nm}$, respectively. The unit cells were the same for all the Au nanoparticles alone and on the Si substrate.

Data availability

The data that support the findings of this study are available from the corresponding author upon reasonable request.

Received: 20 August 2018 Accepted: 23 May 2019

Published online: 20 June 2019

References

- Hu, L. & Chen, G. Analysis of optical absorption in silicon nanowire arrays for photovoltaic applications. *Nano Lett.* **7**, 3249–3252 (2007).
- Noffsinger, J., Kioupakis, E., Van de Walle, C. G., Louie, S. G. & Cohen, M. L. Phonon-assisted optical absorption in silicon from first principles. *Phys. Rev. Lett.* **108**, 167402 (2012).
- Schaadt, D. M., Feng, B. & Yu, E. T. Enhanced semiconductor optical absorption via surface plasmon excitation in metal nanoparticles. *Appl. Phys. Lett.* **86**, 063106 (2005).
- Atwater, H. A. & Polman, A. Plasmonics for improved photovoltaic devices. *Nat. Mater.* **9**, 205 (2010).
- Goykhman, I., Desiatov, B., Khurgin, J., Shappir, J. & Levy, U. Locally oxidized silicon surface-plasmon Schottky detector for telecom regime. *Nano Lett.* **11**, 2219–2224 (2011).
- Kelzenberg, M. D. et al. Enhanced absorption and carrier collection in Si wire arrays for photovoltaic applications. *Nat. Mater.* **9**, 239 (2010).
- Jung, J., Trolle, M. L., Pedersen, K. & Pedersen, T. G. Indirect near-field absorption mediated by localized surface plasmons. *Phys. Rev. B* **84**, 165447 (2011).
- Yamaguchi, M. & Nobusada, K. Indirect interband transition induced by optical near fields with large wave numbers. *Phys. Rev. B* **93**, 195111 (2016).
- Yatsui, T., Yamaguchi, M. & Nobusada, K. Nano-scale chemical reactions based on non-uniform optical near-fields and their applications. *Prog. Quantum Electron.* **55**, 166–194 (2017).
- Noda, M., Iida, K., Yamaguchi, M., Yatsui, T. & Nobusada, K. Direct wave-vector excitation in an indirect-band-gap semiconductor of silicon with an optical near-field. *Phys. Rev. Appl.* **11**, 044053 (2019).
- Hutter, E. & Fendler, J. H. Exploitation of localized surface plasmon resonance. *Adv. Mater.* **16**, 1685–1706 (2004).
- Maier, S. A. *Plasmonics: Fundamentals and Applications*. (Springer, New York, 2007).

13. Irvin, J. C. Resistivity of bulk silicon and of diffused layers in silicon. *Bell Syst. Tech. J.* **41**, 387–410 (1962).
14. Link, S. & El-Sayed, M. A. Spectral properties and relaxation dynamics of surface plasmon electronic oscillations in gold and silver nanodots and nanorods. *J. Phys. Chem. B* **103**, 8410–8426 (1999).
15. Myroshnychenko, V. et al. Modelling the optical response of gold nanoparticles. *Chem. Soc. Rev.* **37**, 1792–1805 (2008).
16. Taflov, A. & Hagness, S. C. *Computational Electrodynamics: The Finite-Difference Time-Domain Method*. (Artech House, Norwood, 2005).
17. Wind, M. M., Vlieger, J. & Bedeaux, D. The polarizability of a truncated sphere on a substrate I. *Phys. A* **141**, 33–57 (1987).
18. Nakayama, K., Tanabe, K. & Atwater, H. A. Plasmonic nanoparticle enhanced light absorption in GaAs solar cells. *Appl. Phys. Lett.* **93**, 121904 (2008).
19. Catchpole, K. R. & Polman, A. Design principles for particle plasmon enhanced solar cells. *Appl. Phys. Lett.* **93**, 191113 (2008).
20. Pillai, S., Catchpole, K. R., Trupke, T. & Green, M. A. Surface plasmon enhanced silicon solar cells. *J. Appl. Phys.* **101**, 093105 (2007).
21. Stuart, H. R. & Hall, D. G. Absorption enhancement in silicon-on-insulator waveguides using metal island films. *Appl. Phys. Lett.* **69**, 2327–2329 (1996).
22. Pankove, J. I. *Optical Processes in Semiconductors*. (Dover, New York, 1971).
23. Loferski, J. J. Theoretical considerations governing the choice of the optimum semiconductor for photovoltaic solar energy conversion. *J. Appl. Phys.* **27**, 777–784 (1956).
24. Wagner, J. & Alamo, J. Ad Band-gap narrowing in heavily doped silicon: a comparison of optical and electrical data. *J. Appl. Phys.* **63**, 425–429 (1988).
25. Richard, S., Aniel, F. & Fishman, G. Energy-band structure of Ge, Si, and GaAs: a thirty-band *k-p* method. *Phys. Rev. B* **70**, 235204 (2004).
26. Bohren, C. F. & Huffman, D. R. *Absorption and Scattering of Light by Small Particles*. (Wiley, Hoboken, 1998).
27. Jackson, J. D. *Classical Electrodynamics*. (Wiley, Hoboken, 1962).
28. Masuko, K. et al. Achievement of more than 25% conversion efficiency with crystalline silicon heterojunction solar cell. *IEEE J. Photovolt.* **4**, 1433–1435 (2014).
29. Fang, C. et al. Germanium-tin alloys: applications for optoelectronics in mid-infrared spectra. *Opto-Electron. Adv.* **1**, 180004 (2018).
30. Tang, L. et al. Nanometre-scale germanium photodetector enhanced by a near-infrared dipole antenna. *Nat. Photonics* **2**, 226 (2008).
31. Chen, X., Zhu, H. & Cai, J. High-performance 4H-SiC-based ultraviolet p-i-n photodetector. *J. Appl. Phys.* **102**, 024505 (2007).
32. Liao, M., Wang, X., Teraji, T., Koizumi, S. & Koide, Y. Light intensity dependence of photocurrent gain in single-crystal diamond detectors. *Phys. Rev. B* **81**, 033304 (2010).
33. Xudong, W. et al. Ultrasensitive and broadband MoS₂ photodetector driven by ferroelectrics. *Adv. Mater.* **27**, 6575–6581 (2015).
34. Joshi, R. K. et al. Hydrogen generation via photoelectrochemical water splitting using chemically exfoliated MoS₂ layers. *AIP Adv.* **6**, 015315 (2016).

Acknowledgements

This work was partially supported by JSPS KAKENHI (Nos. JP18H01470, JP18H05157, JP17H01262, JP15H05760 and JP18H05329), a MEXT as a social and scientific priority issue (Creation of new functional devices and high-performance materials to support next-generation industries; CDMSI) to be tackled by using post-K computer (ID: hp170250), a MEXT Nanotechnology Platform (No.12024046), Japan (JSPS)-France (MAEDI) Bilateral Program SAKURA, the JSPS Core-to-Core Program (A. Advanced Research Networks), Asahi Glass Foundation, and Research Foundation for Opto-Science and Technology.

Author contributions

T.Y. planned the project. S.O., T.T., T.S. and K.S. fabricated Si device and evaluated the photo-sensitivity. T.O., S.C. and S.M. handled the experiment involving measurement of the photo-sensitivity. M.N., K.Y., K.I. and K.N. provided theoretical support for this study. All authors discussed the results. T.Y. wrote the manuscript. All authors reviewed the manuscript.

Additional information

Supplementary information accompanies this paper at <https://doi.org/10.1038/s42005-019-0173-1>.

Competing interests: The authors declare no competing interests.

Reprints and permission information is available online at <http://npg.nature.com/reprintsandpermissions/>

Publisher's note: Springer Nature remains neutral with regard to jurisdictional claims in published maps and institutional affiliations.



Open Access This article is licensed under a Creative Commons Attribution 4.0 International License, which permits use, sharing, adaptation, distribution and reproduction in any medium or format, as long as you give appropriate credit to the original author(s) and the source, provide a link to the Creative Commons license, and indicate if changes were made. The images or other third party material in this article are included in the article's Creative Commons license, unless indicated otherwise in a credit line to the material. If material is not included in the article's Creative Commons license and your intended use is not permitted by statutory regulation or exceeds the permitted use, you will need to obtain permission directly from the copyright holder. To view a copy of this license, visit <http://creativecommons.org/licenses/by/4.0/>.

© The Author(s) 2019